RSC Advances

PAPER

View Article Online
View Journal | View Issue

Cite this: *RSC Adv.*, 2024, **14**, 5400

Enhanced visible light photocatalytic activity of octopod Ag_3PO_4 microcrystals with high index crystal faces†

Liang Ma,[a] Honghua Zhang, *[a] Fuhua Wu,[b] Weilu Zheng,[a] Changchen Li[b] and Junhuai Xiang *[b]

Received 3rd September 2023
Accepted 1st February 2024

DOI: 10.1039/d3ra05996k

rsc.li/rsc-advances

Novel octopod shaped Ag_3PO_4 microcrystals were successfully fabricated by a simple ion exchange method under the conditions of a hot water bath using $[Ag(NH_3)_2]^+$ solution and Na_2HPO_4 solution as the precursors. Meanwhile, sphere and cube shaped Ag_3PO_4 microcrystals were also prepared followed by changing reaction materials as well as temperature. The surface morphology, microstructure and photocatalytic performance were investigated on the three different shaped crystals respectively. Compared to sphere and cube counterparts, the obtained octopod shaped Ag_3PO_4 crystals possess 8 symmetric feet with sharp tips and exhibit higher photocatalytic activity and better cycle stability. After further exploring its formation process, UV-vis diffusion reflectance properties as well as photocurrent transient response, it was found that the Ag_3PO_4 octopod had exposed high index crystal faces, and possessed a narrow band gap as well as high photoexcited transient charge separation efficiency. The results show that the improved photocatalytic activity of octopod shaped Ag_3PO_4 is mainly due to the synergistic action of the strong light absorption capacity and high carrier separation efficiency. These results highlight the tremendous practical application of octopod Ag_3PO_4 microcrystals in visible light photocatalysis.

1. Introduction

In recent decades, increasingly environmental pollution brings serious harm to human survival and health. Meanwhile, fossil energy shortages have aroused widespread concern around the world. In order to solve these problems and realize the sustainable development of modern civilized society, it is urgent to develop effective technologies to remedy the deterioration of the natural environment and explore new alternative clean energy sources.[1–4] Compared with other traditional methods, semiconductor photocatalysis technology has the advantages of simple, recyclability, and high efficiency, and is used widely for antibacterial, deodorization, self-cleaning *etc.*[5–8]

As a promising visible light catalyst, Ag_3PO_4 crystals have always attracted people's attention.[9–12] A variety of approaches such as solution phase precipitation, conventional hydrothermal and impregnation methods have been reported to fabricate spherical, cubic or dodecahedral shaped microcrystal particles.[13–16] The obtained crystals expose almost all low-index crystal faces such as {100}, {110}, and have specific photocatalytic properties. More significantly, high-index facets possess high-density atomic steps, protrusions and kinks, which could be regarded as catalytic active center. Factually, it is proven that crystals terminated by high-index facets have stronger catalytic activity than their low-index facet counterparts. Tan claimed that the dispersing of {111} facet valence band and conduction band facilitates the separation of photogenerated electrons and holes, which improved the Ag_3PO_4 crystal photocatalytic activity.[17] Likewise, Tang *et al.* found that among three facets of {100}, {110} and {111} of Ag_3PO_4 crystal, the {111} facet possesses the highest surface energy. The high surface energy is useful to improve photocatalytic ability in dye degradation.[18] Bi *et al.* used heteroepitaxial technology to prepare TOH Ag_3PO_4 microcrystals with {221} and {332} high refractive index surfaces.[19] And the results indicated that the photocatalytic performance of TOH Ag_3PO_4 on organic pollutants under visible light irradiation is much higher than that of cubes. Therefore, it is a promising way to promote the catalytic performance of photocatalysts by accurately tuning the size and exposed facet of Ag_3PO_4 catalyst. Meanwhile, lots of efforts have been devoted to synthesis of noble metals including Au, Pt, Pd micro/nano crystals with various shapes such as sphere, cube, tetrahedron *etc.*[20–22] Interestingly, a series of octopod shaped nanoparticles of Au–Pd, Pt–Cu, Ag, Al single metals or alloys were fabricated, and these obtained nanoparticles exhibit good

[a]*School of Materials and Energy, Jiangxi Science and Technology Normal University, Nanchang 330013, P. R. China. E-mail: 15270008537@163.com*

[b]*Jiangxi Key Laboratory of Surface Engineering, Jiangxi Science and Technology Normal University, Nanchang 330013, P. R. China. E-mail: xiangjunhuai@163.com*

† Electronic supplementary information (ESI) available. See DOI: https://doi.org/10.1039/d3ra05996k

applications such as electro-catalysis, sensing, photodetection.[23–26]

Bi *et al.* prepared rhombic dodecahedron Ag_3PO_4 and cube Ag_3PO_4 and calculated the specific surface energy, rhombic dodecahedron Ag_3PO_4 {110} surface energy (1.31 J m^{-2}) and cube Ag_3PO_4 {100} surface energy (1.12 J m^{-2}).[27] Yan *et al.* prepared Ag_3PO_4/In_2S_3 composite photocatalyst by simple precipitation method, which showed good adsorption capacity and photocatalytic activity in reducing various organic pollutants in aqueous solution under visible light irradiation.[28] Liu *et al.* prepared highly efficient and stable Ag/Ag_3PO_4 by pyridine-assisted one-pot hydrothermal method, which showed highly efficient and stable photocatalytic activity of methyl orange (MO) and phenol under visible light irradiation.[29] But to our best knowledge, the preparation and property of Ag_3PO_4 crystal with octopod shape is unprecedented by other researchers. Due to its high surface energy, the crystal surface with high refractive index is easy to be quickly eliminated in the process of crystal growth. The simple synthesis of high refractive index faceted semiconductor photocatalysts and the exploration of their potential applications still remains a challenge.

Herein, a simple and green ion exchange method was developed to fabricate different shaped Ag_3PO_4 particles without adding any organic solvents or capping agents. Sphere, cube and octopod shaped Ag_3PO_4 particles were synthesized successively by altering the hydrothermal temperature of the reaction. Subsequently, UV-vis diffusion reflectance properties as well as photocurrent transient response were measured, and the mechanism of improved visible light photocatalytic activity was explored. These results highlight the enormous practical application of octopod Ag_3PO_4 microcrystals in visible light photocatalysis.

2. Experimental

2.1 Materials

The reagents used in the experiment, such as ammonia ($NH_3 \cdot H_2O$), silver nitrate ($AgNO_3$), and absolute ethanol (C_2H_5OH) were purchased from Xilong Science Co., Ltd Anhydrous sodium dihydrogen phosphate (Na_2HPO_4), methylene blue trihydrate ($C_{16}H_{18}ClN_3S_3 \cdot H_2O$), *tert*-butanol, 1,4-benzoquinone, and triethanolamine were bought from Sinopharm Chemical Reagent Co., Ltd. All the used chemical reagents are of analytical grade and no further purification is required. The water used in all experiments was ultrapure grade (18.2 MΩ cm).

2.2 Synthesis of Ag_3PO_4 crystal particles with three different shapes

The specific synthesis process of Ag_3PO_4 crystalline particles with various shapes was described in our previous article.[30] In this part, the main fabrication conditions and parameters were described in brief as follows. In the dark at room temperature (25 °C), 2 mL 0.45 M $AgNO_3$ solution was poured into a beaker containing 200 mL deionized water, then added dropwise 1 mL, 0.15 M NaH_2PO_4 solution, the mixed solution was kept stirring for 30 min, and then centrifuge, some yellow precipitates appeared at the bottom of the centrifuge tube, washed with EtOH and deionized water several times, and then placed in a vacuum to dry at 60 °C for 12 h, the sphere shaped Ag_3PO_4 particles were obtained. Similarly, under dark conditions at room temperature (25 °C), 2 mL 0.45 M $AgNO_3$ solution was put into a beaker, and a certain amount of diluted ammonia water was dropped slowly until a transparent solution was formed exactly. Then, 2 mL 0.15 M Na_2HPO_4 solution was dropped into the above $[Ag(NH_3)_2]^+$ solution under stirring conditions for 30 min. After centrifuged, the obtained yellow precipitates were washed with EtOH and deionized water several times, and then placed in a vacuum to dry at 60 °C 12 h. Resultly, the cube shaped Ag_3PO_4 particles were obtained. Interestingly, under the conditions of darkness and hot water bath temperature (60 °C), 2 mL 0.45 M $AgNO_3$ solution was put in a beaker, and diluted ammonia water was added dropwise, stirred quickly until transparent solution was formed exactly. After that, 200 μL 0.15 M Na_2HPO_4 solution was added dropwise into the $[Ag(NH_3)_2]^+$ solution under stirring conditions for 30 min. After centrifuged, the obtained yellow precipitates were washed with EtOH and deionized water several times, and then placed at room temperature and vacuum dry for 12 h, the octopod shaped Ag_3PO_4 particles were obtained.

2.3 Characterization

The morphology, composition and structure of the obtained Ag_3PO_4 materials was investigated by field emission scanning electron microscopy (FESEM, Zeiss, Sigma) with an energy dispersive spectrum (EDS), X-ray diffractometer (XRD, Shimadzu, Japan), respectively. UV-vis diffuse reflectance spectroscopy (UV-vis DRS, PerkinElmer, USA) was recorded with wavelength range of 200–800 nm on a lambda 750 spectrophotometer using $BaSO_4$ as the reference. The photoluminescence spectra (PL, Zolix, China) were measured at room temperature excited at 325 nm using a ZLX-FS fluorescence spectrometer.

Electrochemical impedance spectroscopy (EIS) was carried out on an electrochemical station (CHI 660E, Chenhua, China). The photocurrent measurement was performed on the same electrochemical workstation with a light on/off cycle of 30 s. They both were conducted in a standard three-electrode system, with a three-electrode system using a three-compartment quartz cell with 0.5 M Na_2SO_4 electrolyte solution (100 mL). A saturated calomel electrode (SCE) and a platinum plate were applied as the reference electrode and counter electrode, respectively. The Ag_3PO_4 powder electrodes on an ITO electrode act as the working electrode. All potentials were recorded according to the saturated calomel electrode.

The photocatalytic activities of Ag_3PO_4 crystals with three different morphologies for methylene blue solution (MB) was evaluated under visible light irradiation by a 500 W Xenon light source (Xujiang Electromechanical Plant, Nanjing, China) equipped with a 420 nm cutoff filter. Experiments were as follows: 30 mg of Ag_3PO_4 photocatalyst was added into 60 mL capacity quartz vessel including 50 mL of MB (10 mg L^{-1}). In order to establish absorption–desorption equilibrium between

the surface of photocatalyst and MB, the suspensions were magnetically stirred in the dark for 60 min before irradiation. At the interval of 10 min, 4 mL of solution was taken out and centrifuged to remove the photocatalyst. The concentration of MB solutions was characterized by using spectrophotometer at the wavelengths of 664.7 nm (Lambda 35, PerkinElmer).

3. Results and discussion

3.1 Morphology and structure of Ag_3PO_4 particles with three different shapes

The surface morphology of the obtained different shaped Ag_3PO_4 particles was observed by SEM, as shown in Fig. 1. When $AgNO_3$ solution is used as the precursor, the produced particles are mainly spherical in shape, but each particle varies slightly in size and the average value is 320 nm (Fig. 1a). Interestingly, when the precursor is replaced with $[Ag(NH_3)_2]^+$ solution, the produced particles become standard cubic shape with a smooth surface and regular corners, and the side length is approximately 2 μm, as shown in Fig. 1b. Continue using $[Ag(NH_3)_2]^+$ solution as the precursor, and keeping the reaction process at 60 °C in a water bath, the obtained particles exhibit novel shape like octopod, and possess 8 symmetric feet with sharp tips and 4 recessed surfaces. The distance between two adjacent feet is about 2 μm, as is shown in Fig. 1c.

The powder XRD patterns of the three kinds of morphologies of Ag_3PO_4 photocatalysts are shown in Fig. 1d. The diffraction peak positions corresponding to the three morphologies of Ag_3PO_4 are consistent with the standard Ag_3PO_4 body-centered cubic card (JCPDS No. 06-0505), and no other diffraction peaks were observed in the XRD patterns, indicating that well crystallised pure phase compounds were synthesized. Additionally, it can be clearly found that the cube and octopod Ag_3PO_4 have different diffraction peak intensity ratios at (110) and (200), and the diffraction peak intensity of the octopod Ag_3PO_4 at (210) is clearly lower than that of two others.

Due to the important role in the photocatalytic reaction, the specific surface area of Ag_3PO_4 with three different morphologies has been tested, as shown in Fig. S1.† The specific surface areas of sphere, cube and octopod Ag_3PO_4 can be calculated as 11.16, 35.47 and 46.65 $m^2\ g^{-1}$, respectively, which indicates the largest specific surface area and best photocatalytic activity for octopod Ag_3PO_4.

3.2 XPS analysis of Ag_3PO_4 particles with three morphologies

The chemical states of three kinds of Ag_3PO_4 samples with different morphologies were studied by XPS. The XPS spectra show the photoelectron peaks of Ag, P, and O elements (Fig. 2a), where Ag, P, and O derive from Ag_3PO_4. Fig. 2b–d shows the characteristic curves of Ag, P and O in Ag_3PO_4. In Fig. 2b, two spectral characteristic peaks of Ag 3d at 374.18 eV and 368.18 eV belong to Ag $3d_{1/2}$ and Ag $3d_{2/3}$, respectively, indicating that Ag in the material exists in the form of Ag^+. In Fig. 2c, P 2p shows a single broad peak at 132.88 eV, indicating that P in the material is present in the form of P^{5+}. In Fig. 2d, the signal peak of 530.78 eV belongs to O 1s, indicating that O in the sample exists in the form of O^{2-}, which proves that no metal Ag is present.

3.3 Visible light photocatalytic activity of Ag_3PO_4 particles with three shapes

The photocatalytic degradation activity of Ag_3PO_4 catalysts with three shapes was evaluated by testing their ability to decompose organic dye methylene blue (MB) under visible light ($\lambda > 420$ nm) at room temperature. Fig. 3a illustrates the actual effect on degradation of MB of three morphologies of Ag_3PO_4 catalysts. The inset of Fig. 3a shows the optical photo of octopod Ag_3PO_4 powder under 0 to 70 min photocatalysis. By observing the color change in the solution from 0 to 70 min, it can be clearly seen that it took the shortest time (less than 20 min) for the MB solution added with octopod Ag_3PO_4 to degrade 80%, followed by cube Ag_3PO_4 and sphere Ag_3PO_4 which indicates the good photocatalytic performance of octopod Ag_3PO_4 in the

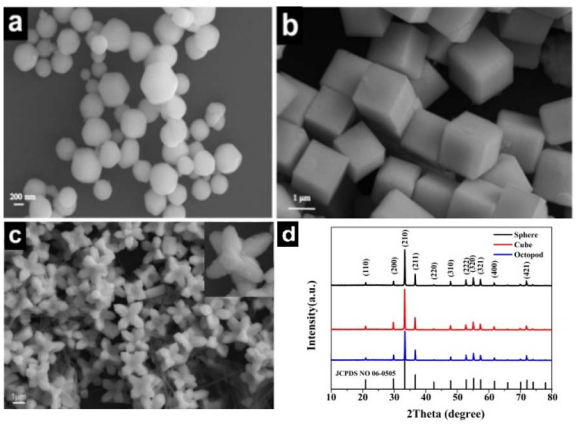

Fig. 1 SEM images (a–c) and XRD patterns (d) of the three shaped Ag_3PO_4 crystals. (a) Sphere (b) cube and (c) octopod.

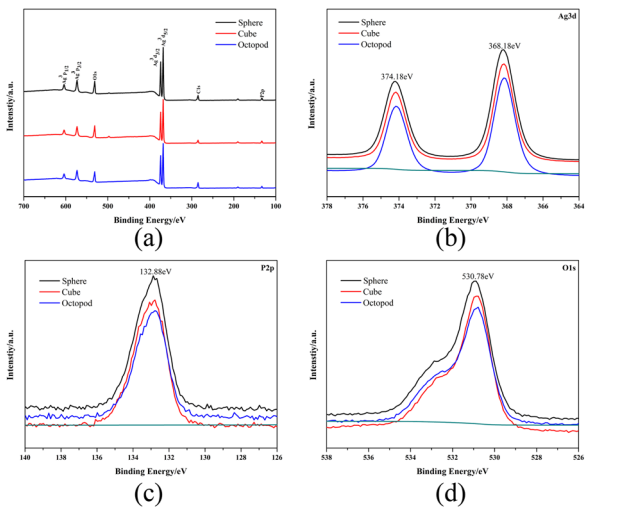

Fig. 2 (a) XPS spectra of Ag_3PO_4. High-resolution XPS spectra of Ag 3d (b), P 2p (c), and O 1s (d) from Ag_3PO_4.

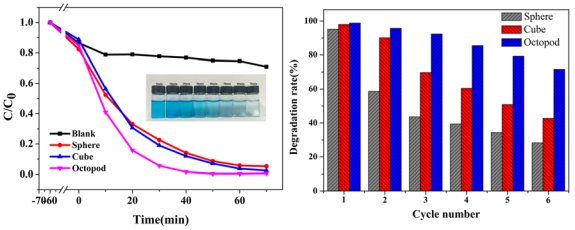

Fig. 3 (a) Photodegradation plots of MB solution with Ag_3PO_4 particles obtained at different time. (b) Cycle stability performance diagram of Ag_3PO_4 particles with three morphologies.

degradation of MB. The concentration of MB does not show obvious decline in blank test indicating that the self-degradation of MB is negligible under visible-light irradiation. The degradation effect is defined as C/C_0, where C and C_0 represents the residual and initial concentration of MB solution, respectively.

In order to evaluate and compare the photostability of silver phosphate photocatalysts with different morphologies, six cycles of batch degradation experiments were carried out with MB as the target pollutant. As shown in Fig. 3b, after six cycles, the photodegradation removal rate of the octopod Ag_3PO_4 photocatalyst for MB is reduced from 98% to 72%, and the removal efficiency of MB by the cube Ag_3PO_4 photocatalyst decreased from 97% to 43%, the degradation rate of the sphere Ag_3PO_4 photocatalyst is greatly reduced to 28%, and the photocatalytic activity is obviously deactivated. All the results show that the octopod shaped Ag_3PO_4 photocatalyst has relatively better photo-corrosion resistance without adding sacrificial agents.

After the stability experiment, we characterized Ag_3PO_4 with three different morphologies by SEM (as shown in Fig. S2†). From Fig. S2a–c,† it can be found that the crystal structure and size of the three morphologies of Ag_3PO_4 did not change after stability experiments. This also indicates that the obtained Ag_3PO_4 has good stability in photocatalysis. Three different morphologies of Ag_3PO_4 were further characterized by XPS. The XPS spectrum shows the photoelectron peaks of Ag, P, and O elements (Fig. S2d†), where Ag, P, and O derive from Ag_3PO_4. Fig. S2e and f† shows the characteristic curves of Ag, P and O in Ag_3PO_4. Fig. S2e,† two spectral characteristic peaks of Ag 3d at 374.28 eV and 368.28 eV belong to Ag $3d_{1/2}$ and Ag $3d_{2/3}$, respectively, indicating that Ag in the material exists in the form of Ag^+. In Fig. S2f,† P 2p shows a single broad peak at 133.78 eV, indicating that P in the material is present in the form of P^{5+}. In Fig. S2g,† the signal peak of 532.28 eV belongs to O 1s, indicating that the O in the sample exists in the form of O^{2-}. All the results show that the octopod Ag_3PO_4 can be well maintained after the experiment.

3.4 Formation mechanism of octopod Ag_3PO_4 microcrystals

Due to unstable properties of Ag_3PO_4, high-resolution transmission electron microscopy cannot be used to analyse its structural characteristics, but it can be studied geometrically based on the simple cube structure of Ag_3PO_4. From the SEM images, it can be judged that the octopod Ag_3PO_4 was formed by growing preferentially along the direction of ⟨111⟩ and ⟨110⟩, and slightly in the direction of ⟨100⟩ of original cube seed crystal. As shown in Fig. 4, by using protractor, the value of angle α was measured about 16°, and a typical crystal index of the octopod Ag_3PO_4 is signed as (2/tan α 2 0). As a result, the crystal index of octopod Ag_3PO_4 is calculated as (720), the calculation method is shown in Fig. S3.† The exposed crystal plane is a high-index crystal plane, which is relative to other low-index crystal planes. The crystal face has higher surface energy and larger specific surface area, so it effectively improves the atom use efficiency, catalytic activity and selectivity of Ag_3PO_4.

3.5 Photocatalytic enhancement mechanism

Optical properties, such as UV-vis diffuse reflectance spectra, photoluminescence (PL) spectroscopy, and the photocurrent transient response analysis were investigated to illustrate the photocatalytic mechanism of octopod shaped Ag_3PO_4. The optical properties of the obtained Ag_3PO_4 photocatalysts were investigated by UV-vis diffuse reflectance spectra. As shown in Fig. 5a, the absorption edge of sphere Ag_3PO_4 sample is near 500 nm, while the absorption edge of cube Ag_3PO_4 is slightly red-shifted (about 515 nm), and the absorption edge of octopod Ag_3PO_4 is further red-shifted (about 525 nm). The octopod crystal has better light response than the other two shape samples, and has a wider absorption range and higher absorption in the visible light range. It's well known that the optical band gap of materials can be calculated from the plot of $\alpha h\nu = A(h\nu - E_g)^{n/2}$ (Fig. 5b). Based on these absorption edges, the corresponding band gaps of Ag_3PO_4 spheres, cubes and octopods is 2.56, 2.50 and 2.46 eV, respectively. Compared with the other two morphologies, the octopod shaped Ag_3PO_4 crystals possess small band gap which bring relatively high visible light energy utilization and can powerfully drive the photocatalytic action on organic pollutants under visible light irradiation degradation.[31–33]

Photoluminescence (PL) spectroscopy is used to evaluate the carrier recombination efficiency and to reveal the separation ability of photogenerated electron–hole pairs of samples. Generally, the lower the photoluminescence intensity, the slower the carrier recombination speed, and the higher the activity of the photocatalytic reaction reveals. As shown in Fig. 5c, the fluorescence intensity of Ag_3PO_4 samples with sphere, cube, and octopod shapes decreases successively,

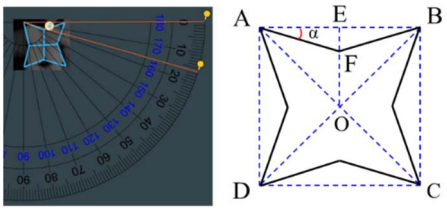

Fig. 4 Crystal orientation of octopod shaped Ag_3PO_4.

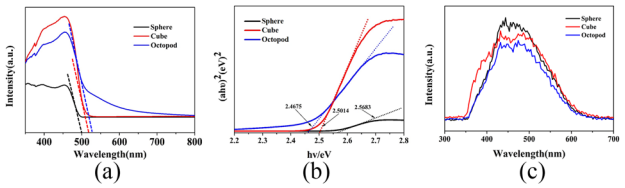

Fig. 5 (a) UV-vis DRS spectra of as-prepared Ag_3PO_4 samples with three shapes and the corresponding band gap (b) as well as PL spectra (c).

indicating that the octopod shaped Ag_3PO_4 possess slower carriers recombination speed and separate the photo-induced electron–hole pairs more quickly.

The photocurrent transient response analysis is the basic test in the photoelectrochemical measurement of materials, and it has been widely used to evaluate the separation ability of photogenerated carriers. The photoexcited transient charge separation efficiency of Ag_3PO_4 samples with different morphologies were evaluated by using the transient photocurrent response test. As shown in Fig. 6a, the value of current density of the octopod shaped Ag_3PO_4 sample is about 0.00017 mA cm^{-2}, and it is obviously higher than that of the cube shaped Ag_3PO_4 sample and sphere shaped sample. In order to further study the charge transfer process, the resistance of charge separation and transfer of Ag_3PO_4 with different morphologies were studied by EIS measurement. In EIS analysis, the arc diameter in the EIS spectrum is generally used to evaluate the interface charge transfer process, where a smaller arc means faster interface charge transfer.[34] Fig. 6b shows that octopod shaped Ag_3PO_4 sample exhibited smaller radius than the cube shaped and sphere shaped samples. It is indicating that a facile charge transfer process took place in octopod shaped Ag_3PO_4 crystal surface, which is consistent with the result of photocurrent response above. Therefore, considering the results of photocurrent response and electrical impedance experiments, the octopod shaped Ag_3PO_4 crystal with this unique structure can significantly improve the separation and transfer efficiency of photogenerated carriers of silver phosphate.

To further clarify the photocatalytic mechanism of octopod shaped Ag_3PO_4, a free radical trapping experiment was carried out on the catalyst. In the MB degradation system of octopod shaped silver Ag_3PO_4, benzoquinone (BQ), triethanolamine (TEOA) and *tert* butanol (TBA) was used as superoxide radicals ($\cdot O^{2-}$), photo-generated holes (h^+) and hydroxyl radicals ($\cdot OH$)

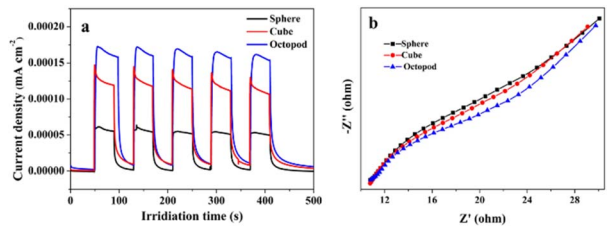

Fig. 6 Photocurrent response (a) and EIS plots (b) of Ag_3PO_4 photocatalyst.

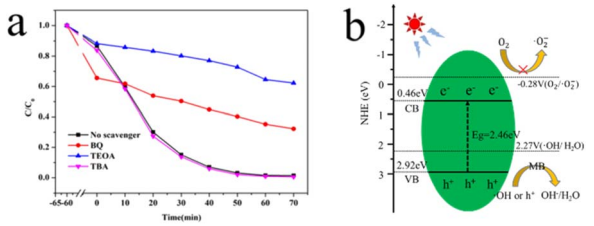

Fig. 7 (a) MB degradation over concave octagon Ag_3PO_4 in the presence of different scavengers, (b) the charge transfer mechanism of octopod shaped Ag_3PO_4.

scavenger, respectively.[35] As shown in Fig. 7a, it is obvious that at 70 min, the TEOA C/C_0 value is the highest, followed by BQ and the lowest is TBA. The degradation rate was significantly reduced in the presence of TEOA and BQ. It can be seen that in the photocatalytic process, holes can directly oxidize MB, while some holes will also react with water to convert to $\cdot OH$, which is similar to the reported literature.[36]

According to the above-mentioned results, the probable photocatalytic activity enhancement mechanism for the charge transfer of octopod shaped Ag_3PO_4 is further proposed based on the energy band structure. As shown in Fig. 7b, the band gaps of octopod shaped Ag_3PO_4 is 2.46 eV, as calculated based on the aforementioned UV-vis DRS spectra, which means that octopod shaped Ag_3PO_4 can adsorb photons and generate e^-–h^+ pairs under visible-light irradiation. Under light excitation, the electrons (e^-) of Ag_3PO_4 migrate from VB to CB, leaving holes (h^+) in VB. The electrons in Ag_3PO_4 react with molecular oxygen dissolved in the solution to generate highly reactive Super oxygen anion. The holes and superoxide anions with strong oxidizing ability quickly transfer to the surface, degrading nearby MB molecules.

4. Conclusions

A new type of octopod shaped Ag_3PO_4 crystals were synthesized by a simple and green ion exchange method. For comparison, sphere and cube Ag_3PO_4 particles were also prepared simultaneously by adjusting reaction materials and hydrothermal temperature. The crystal plane exposed by the octopod shaped Ag_3PO_4 particles is a high-index facet calculated as (2/tan α 2 0). Compared with the other two morphologies, the octopod shaped Ag_3PO_4 crystals possess small band gap with 2.46 eV, which bring relatively high visible light energy utilization, and the unique structure can significantly improve the separation and transfer efficiency of photogenerated carriers of silver phosphate. Furthermore, the octopod shaped Ag_3PO_4 crystals exhibit excellent photocatalytic performance in the degradation of methylene blue MB aqueous solution. The photodegradation rates on MB can reach 99.7% within 60 min under the visible light irradiation. The enhanced efficiency of visible light photocatalysis may be due to the stronger visible light absorption capacity and the effective separation and transfer of carriers. The radical trapping experiments further confirmed that the active species of holes played the crucial role in the

photocatalytic degradation of antibiotic pollutants by using octopod shaped Ag_3PO_4 as the photocatalyst. This work highlights the effect of crystal face exposure on the photocatalytic degradation of organics by Ag_3PO_4, and expected to provide new guidance on enhanced visible light photocatalytic activity Ag_3PO_4 photocatalyst.

Conflicts of interest

There are no conflicts to declare.

Acknowledgements

The authors acknowledge the financial support from the National Natural Science Foundation of China (Grants No. 52063015, 51861008), The Jiangxi Provincial Natural Science Foundation (20212BAB204018).

Notes and references

1 Q. Fu, C. C. Long, L. F. Qin, Z. X. Jiang, T. P. Qing, P. Zhang and B. Feng, *Environ. Pollut.*, 2021, **283**, 117109.
2 R. Balaji, S. Maheshwaran, S. M. Chen, E. Tamilalagan, N. Chandrasekar, S. Ethiraj and M. S. Samuel, *Environ. Pollut.*, 2022, **296**, 118754.
3 S. Panimalar, S. Logambal, R. Thambidurai, C. Inmozhi, R. Uthrakumar, A. Muthukumaran and K. Kaviyarasu, *Environ. Res.*, 2022, **205**, 112560.
4 M. R. Rajeshwari, S. Kokilavani and S. S. Khan, *Chemosphere*, 2022, **291**, 132735.
5 A. l. Soliman, A. M. A. Abdel-Wahab and H. N. Abdelhamid, *RSC Adv.*, 2022, **12**, 7075–7084.
6 H. S. Alanazi, N. Ahmad and F. A. Alharthi, *RSC Adv.*, 2023, **58**, 2506–2524.
7 C. Liu and J. Rouhi, *RSC Adv.*, 2021, **11**, 9933–9941.
8 Y. X. Dai, Y. T. Wang, G. C. Zuo, J. J. Kong, Y. Guo, C. Sun and Q. M. Xian, *Chemosphere*, 2022, **293**, 133575.
9 H. He, M. N. Guo, J. Cao, H. L. Lin and S. F. Chen, *Mater. Lett.*, 2019, **244**, 54–57.
10 S. H. Tong, Z. B. Liu, Y. Lin and C. P. Yang, *Int. J. Environ. Res. Public Health*, 2022, **19**, 14865.
11 Z. Xu, J. Zhong, M. Li and H. Yang, *Mater. Lett.*, 2022, **323**, 132544.
12 C. M. Yu, X. J. Chen, N. Li, Y. Zhang, S. L. Li, J. M. Chen, L. Yao, K. C. Lin, Y. Q. Lai and X. R. Deng, *Environ. Sci. Pollut. Res.*, 2022, **29**, 18423–18439.
13 N. N. Fulzele, B. A. Bhanvase and S. L. Pandharipande, *Mater. Chem. Phys.*, 2022, **292**, 126809.
14 A. Amirulsyafiee, M. M. Khan, M. Y. Khan, A. Khan and M. H. Harunsani, *Solid State Sci.*, 2022, **131**, 106950.
15 N. Wang, J. Wang, Q. Y. Zhao, C. Y. Ge, B. R. Hou, Y. T. Hu and Y. L. Ning, *J. Photochem. Photobiol., A*, 2022, **432**, 114110.
16 D. S. Li, Y. Liu, Y. T. Yang, G. G. Tang and H. Tang, *Appl. Catal., B*, 2019, **245**, 71–86.
17 B. J. Zheng, X. Wang, C. Liu, K. Tan, Z. X. Xie and L. S. Zheng, *J. Mater. Chem. A*, 2013, **1**, 12635–12640.
18 D. J. Martin, N. Umezawa, X. W. Chen, J. H. Ye and J. W. Tang, *Energy Environ. Sci.*, 2013, **6**, 3380–3386.
19 Z. B. Jiao, Y. Zhang, H. C. Yu, G. X. Lu, J. H. Ye and Y. P. Bi, *Chem. Commun.*, 2012, **49**, 636–638.
20 X. W. Li, X. Zhou, H. Guo, C. Wang, J. Y. Liu, P. Sun, F. M. Liu and G. Y. Lu, *ACS Appl. Mater. Interfaces*, 2014, **6**, 18661–18667.
21 G. H. Han, X. Y. Xiao, J. Hong, K. J. Lee, S. Park, J. P. Ahn, K. Y. Lee and T. Yu, *ACS Appl. Mater. Interfaces*, 2020, **12**, 6328–6335.
22 P. R. Mendoza and G. Guisbiers, *Nanotechnology*, 2019, **30**, 305702.
23 M. Zhang, Y. Xu, S. Q. Wang, M. Y. Liu, L. B. Wang, Z. Q. Wang, X. N. Li, L. Wang and H. J. Wang, *J. Mater. Chem. A*, 2021, **9**, 13080–13086.
24 S. S. Wang, W. J. Qiu, T. P. Wang and C. L. Lee, *Appl. Surf. Sci.*, 2022, **605**, 154670.
25 Y. Kim, Y. W. Lee, S. Lee, J. Gong, H. S. Lee and S. W. Han, *ACS Appl. Mater. Interfaces*, 2021, **13**, 45538–45546.
26 X. Liu, K. K. Wang, L. M. Zhou, H. K. Pu, T. Zhang, J. Jia and Y. J. Deng, *ACS Sustain. Chem. Eng.*, 2020, **8**, 6449–6457.
27 Y. P. Bi, S. X. Ouyang, N. Umezawa, J. Y. Cao and J. H. Ye, *J. Am. Chem. Soc.*, 2011, **133**, 6490–6492.
28 T. J. Yan, J. Tian, W. F. Guan, Z. Qiao, W. J. Li, J. M. You and B. B. Huang, *Appl. Catal., B*, 2017, **202**, 84–94.
29 Y. P. Liu, L. Fang, H. D. Lu, Y. W. Li, C. Z. Hu and H. G. Yu, *Appl. Catal., B*, 2012, **115**, 245–252.
30 F. H. Wu, T. Wu, M. Wang, J. H. Xiang and H. H. Zhang, *J. Jiangxi Sci. Technol. Norm. Univ.*, 2020, **06**, 20–25.
31 S. Chattopadhya, S. Mondal and G. De, *J. Mater. Chem. A*, 2017, **5**, 17341–17351.
32 Y. Liang, Z. K. Xiang, X. J. Zhao, F. F. Xiang, P. P. Yan, T. Yu, X. Li and Y. Yang, *CrystEngComm*, 2022, **24**, 3865–3871.
33 M. S. Hsieh, H. J. Su, P. L. Hsieh, Y. W. Chiang and H. M. Huang, *ACS Appl. Mater. Interfaces*, 2017, **9**, 39086–39093.
34 H. M. Zhang, J. He, C. Y. Zhai and M. S. Zhu, *Chin. Chem. Lett.*, 2019, **30**, 367–371.
35 U. Sulaeman, D. Hermawan, R. Andreas, A. Z. Abdullah and S. Yin, *Appl. Surf. Sci.*, 2018, **428**, 1029–1035.
36 D. S. Li, Y. Liu, Y. T. Yang, G. G. Tang and H. Tang, *J. Colloid Interface Sci.*, 2022, **608**, 2549–2559.